Ore Geology Reviews 92 (2018) 613–626

Contents lists available at ScienceDirect

Ore Geology Reviews

journal homepage: www.elsevier.com/locate/oregeorev

Geological, geochemical and fluid inclusion studies on the evolution of barite mineralization in the Badroud area of Iran

Zahra Alaminia*, Mortaza Sharifi

Department of Geology, Faculty of Sciences, University of Isfahan, Azadi Square, P.O. Box 81746-73441, Isfahan, Iran

ARTICLE INFO

Keywords:
Barite geochemistry
Fluid inclusion
Urumieh–Dokhtar Magmatic Arc
Iran

ABSTRACT

A sequence of andesitic to dacitic volcanic and volcano-sedimentary rocks from the Late Eocene in the central part of the Urumieh–Dokhtar Magmatic Arc (UDMA) hosts a number of barite occurrences. The Badroud barite deposit is economically important deposit in the study area. The petro-geochemical characteristics of the deposit indicate that the least-altered volcanic host rock was produced as orogenic volcanic rock in the continental margin arc setting. It displays characteristics of a high-K and calc-alkaline series. Mineralized host rock mostly consists of barite crystals, and subordinate quartz, calcite, gypsum, fluorite and rare pyrite, chalcopyrite, galena, stibnite and cinnabar minerals. Petrographic studies revealed three types of barite. The early stage barite occurs as stockworks of large tabular and bladed crystals trending NW-SE in dextral strike-slip faults. The second stage barite precipitated as thick lensoid veins (50 × 3 m) of medium tabular crystals extending in a N-S direction. The third stage of barite mineralization occurs as thin acicular veins trending in a NW-SE direction. Chemically, the barite deposit is characterized by the low amounts of Sr, K, Ca and low Sr/Ba ratio. Fluid inclusion studies, applied to the first stage of bladed crystals of barite veinlets, show a high homogenization temperature of 256–338 °C and 8–13% (wt.) NaCl eq. salinity. Fluid inclusions in the second stage of barite mineralization are characterized by low salinity of 1–9% (wt.) NaCl eq. at a 160–214 °C homogenization temperature. The fluid inclusions occurring in the third stage of thin barite veins revealed high salinity of 19% (wt.) NaCl eq. with a 166–212 °C homogenization temperature. The fluid inclusion characteristics of the first stage barite show a hydrothermal origin with a deeper-seated source on the seafloor associated with a lower sequence of the Late Eocene felsic rock. The second stage barite, exposed beneath the upper sequence of Late Eocene andesite, was formed due to increased dilution, possibly with seawater. The third stage barite mineralization is associated with saline water and the interaction of fluid with volcanic and conglomerate host rocks. The obtained data show that the mineralization at Badroud barite deposit is similar to the Kuroko-type massive sulfide deposits in an arc setting.

1. Introduction

There are two major metallogenic belts of barite mineralization on both sides of the Urumieh–Dokhtar magmatic arc (UDMA) in Isfahan province of Iran. They are named as Malayer-Isfahan and Qom-Kashan belts, and respectively located in the western and the eastern parts of the UDMA (Fig. 1a). The subordinate barite mineralization in Iran-Kuh, Mehdi-Abad, Angouran and Ravanj Mississippi valley-type Pb-Zn deposits in Malayer-Isfahan barite belt, within the Sanandaj–Sirjan zone, is associated with Mesozoic carbonate rocks (e.g., Ghazban et al., 1994; Gheshlaghi, 2002; Ghasemi et al., 2008; Rajabi et al., 2012; Nejadhadad et al., 2016), whereas, the major barite mineralization in Tappeh-Sorkh and Rangan deposits in the Qom-Kashan barite belt mainly formed in the Cenozoic volcanics of the back arc basin of the UDMA (e.g., Khalaj-Masoumi et al., 2009; Taghipour et al., 2010; Hashemi, 2016).

In the past decade in the eastern part of the UDMA near Kashan, several small barite deposits have been discovered and mined (Fig. 1b). But on the barite deposits associated with volcanic rocks, very few studies have been carried out so far. The Kuh-e Latif geologic map (1:100000 scale) shows that most barite deposit hosted by volcanic rocks were emplaced between the Late Eocene to the Oligocene (Nabavi and Houshmandzadeh, 1984). Parsapoor et al. (2009) and Taghipour et al. (2010) studied Rangan rhyolite-hosted barite (70 km NW of Isfahan) using stable isotope studies of alteration minerals. These studies revealed that the Qom–Zefreh dextral strike-slip fault with a NW-SE trend has served as a feeder channel and barite mineralization at Rangan was related to deep magmatic-hydrothermal fluids. Khalaj-Masoumi et al. (2009) studied the Delijan barite deposit and

* Corresponding author.
E-mail address: z.alaminia@sci.ui.ac.ir (Z. Alaminia).

https://doi.org/10.1016/j.oregeorev.2017.12.011
Received 2 August 2017; Received in revised form 19 November 2017; Accepted 8 December 2017
Available online 08 December 2017
0169-1368/

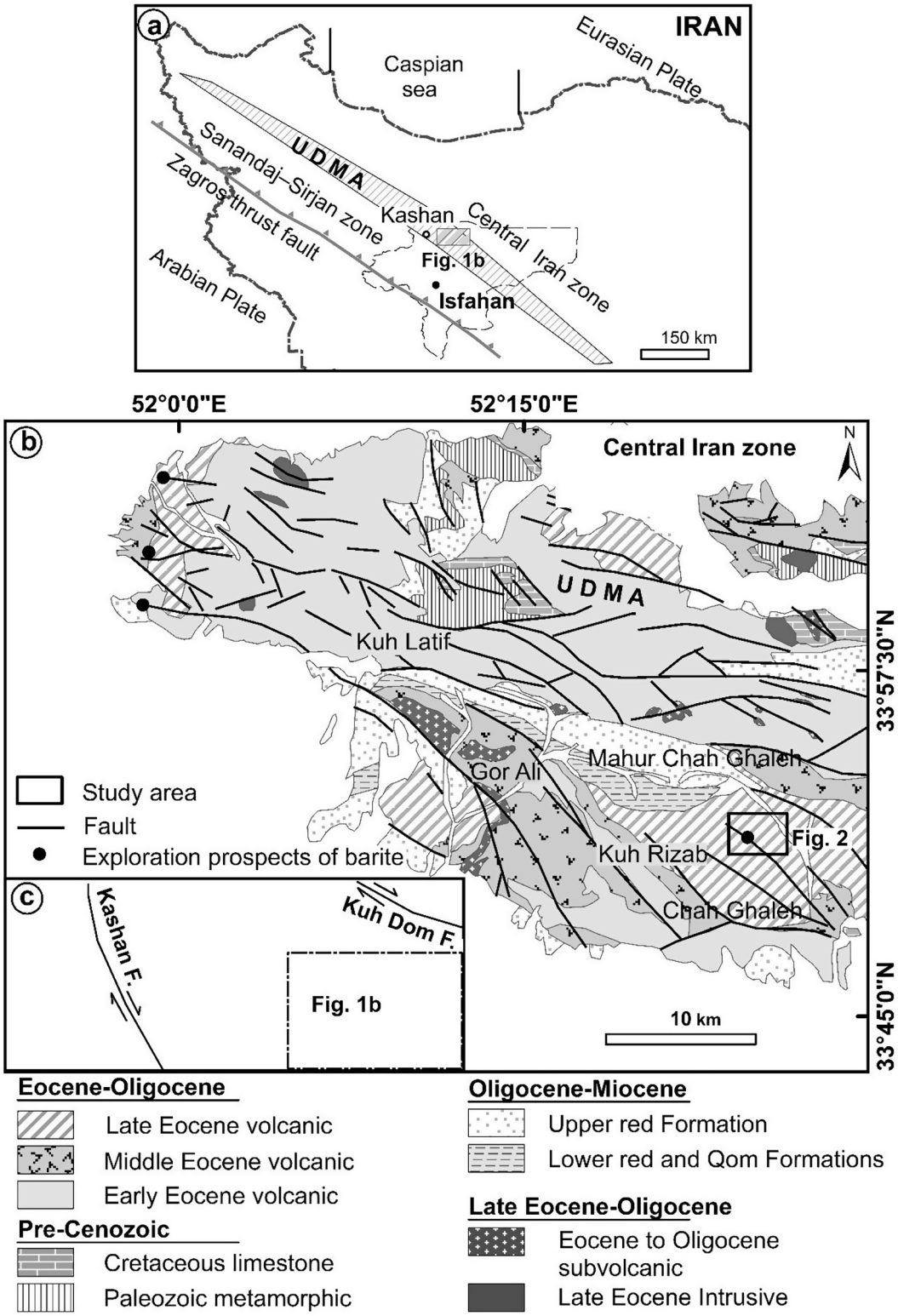

Fig. 1. (a) Structural map of Iran showing the extent of the UDMA from northwest to southeast between Sanandaj-Sirjan and Central Iran zones. Site location of Badroud area in east of Kashan (north of Isfahan). (b) Regional geologic map based on Kashan and Aran maps (1:250000 scale) and Kuh-e Latif map (1:100000 scale). Note to the distribution of barite occurrences. (c) The Badroud area between two dextral strike-slip faults: Kuh-e Dom fault to the north and Kashan to the west. Kashan fault is the major branch of the Qom-Zefreh fault.

determined the type of ore body using fluid inclusion studies. Hashemi (2016) studied on a similar barite deposit about 60 km east of Kashan town and proposed it to be of the Kuroko-type deposit. It was also determined that the homogenization temperature of fluid inclusions was 148–372 °C in barite minerals.

The Badroud barite deposit, located near the Kashan, is one of the few deposits in this area, which with 1.83 million tonnes is considered as economic potential. There are 23 veins as well as several barite lenses at Badroud deposit. Three styles of barite mineralization have been recognized in this area. Because of the abundant barite formations, investigation of the shape and geochemistry of the different barites can be determined for geological reconstruction and

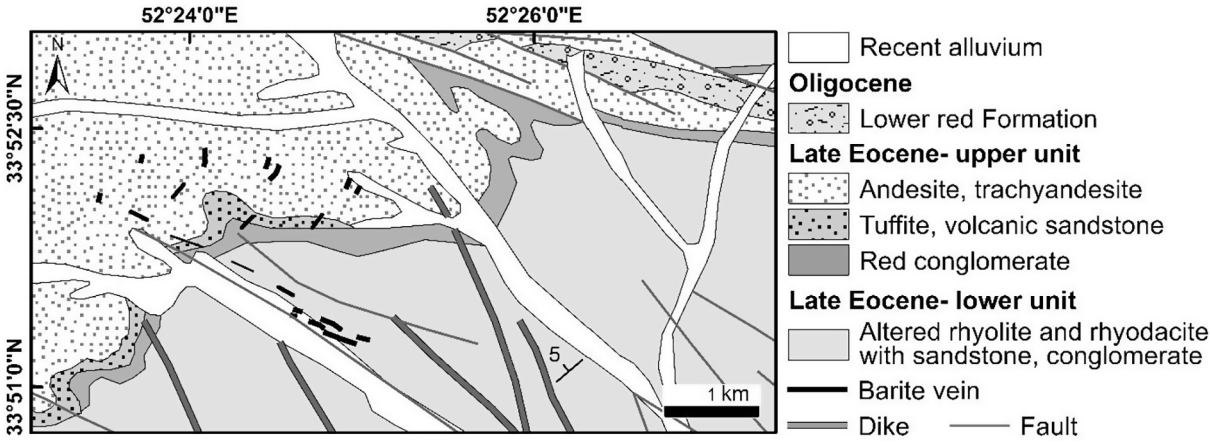

Fig. 2. Position of barite veins in the geologic map of Badroud deposit. Modified after Nabavi and Houshmandzadeh (1984).

hydrothermal studies (e.g., Hanor, 2000; Kontak et al., 2006; Pfaff et al., 2010; Griffith and Paytan, 2012; Revan et al., 2014; Torró et al., 2016). The current research presents the geochemical characteristics of the volcanic host rock and morphological properties of the barite minerals at Badroud deposit. It also presents a description of the physico-chemical conditions of fluid inclusion in barite minerals. The main objective is to provide palaeo-environmental evolution of barite in the Badroud area that might be useful for exploration on a regional scale along back region of the UDMA.

2. Geology

2.1. Regional geology

The UDMA is located in the northeastern margin of the Zagros orogenic belt between the Sanandaj–Sirjan zone and the central Iran and features a NW-SE direction (Alavi, 2004) (Fig. 1a). During the Zagros collision, a number of developed faults accompanied by mafic to felsic magmatism (Aghanabati, 1986). The Cenozoic magmatic activities of the UDMA are related to northward subduction of the Neo-Tethys oceanic crust during continued convergence of the Arabian plate with the Eurasian plate (e.g., Forster et al., 1972; Berberian et al., 1982; Sengor, 1987; Omrani et al., 2008; Azizi et al., 2011). The subduction–collision event led to extensive continental volcanism within the UDMA with several back arc basins behind this volcanic arc (Verdel, 2009; Ghasemi et al., 2011). However, some researchers propose an island arc setting for the UDMA (e.g., Alavi, 1996; Ghorbani, 2006; Shahabpour, 2007; Ghorbani and Bezenjani, 2011).

The Badroud barite deposit is located about 90 km east of Kashan (Fig. 1a). Tectonically, the Badroud area lies in the back region of the UDMA (Fig. 1a) and belongs to the Qom-Kashan barite belt. The basement of the Badroud area comprises the small bodies of the Paleozoic metamorphic rocks that mainly consist of schist, phyllite and crystalized limestone (Amidi and Zahedi, 1975; Fig. 1b). The Late Cretaceous limestone and marl units occur in the north and the northwest of Mahour Chah Ghaleh village (Fig. 1b). The Eocene volcanics have been exposed in a large area extending from northwest of Kuh-e Latif to the southeast of Kuh-e Rizab (Fig. 1b). Previous works have identified marine fossils dominated by an Eocene pulse of the UDMA that shows the volcanism was largely shallow marine (e.g., Stocklin, 1968; Berberian and King, 1981). The Kuh-e Latif geologic map (1:100000 scale) classifies the types of volcanic rock as the Early Eocene, the Middle Eocene and the Late Eocene (Nabavi and Houshmandzadeh, 1984).

The Early Eocene volcanic rocks consist largely of tuff with basaltic andesite, rhyolite and rhyodacite composition from the base to the top and ignimbrite accompanied by a few interbeds of sandstone and limestone. The Middle Eocene volcanics comprise tuffite, rhyolite ash tuff, sandstone, conglomerate, shale and limestone (Amidi and Zahedi, 1975). The Late Eocene volcanics (please see Section 2.2) non-conformably occur on the Middle Eocene volcanic and tuff units. They predominately contain rhyolite and rhyodacite tuff to andesite, basaltic andesite and volcanic sandstone. These rocks are locally present in four locations on the map (Fig. 1b).

The Badroud barite deposit is hosted by the Late Eocene volcano-sedimentary rocks that are exposed in the southern Mahour Chah Ghaleh village (Fig. 1b). The narrow outcrops of the Eocene sub-volcanics are situated in the west of Gor Ali and the north of Mahur Chah Ghaleh (Fig. 1b). They comprise rhyodacite porphyries which are overlain by the Oligocene to the Miocene sedimentary rocks. Poorly developed the Late Eocene intrusions of granodiorite occur in the north. They are generally less than several kilometers in size. Some igneous rocks occurring between Kashan and Natanz, have been dated, including andesite dating (33 Ma) and diorite dating (16 Ma) using the zircon U-Pb method (Chiu et al., 2013).

The youngest sedimentary series at regional scale are divided into three major sedimentary sequences: 1) the Lower Red Formation; 2) the Qom Formation; and 3) the Upper Red Formation. Lithologically, they are composed of red marl, conglomerate and sandstone that are Oligocene in age, organic-detrial limestone, marl and gypsum belonging to the Oligocene-Miocene as well as sandstone, conglomerate and marl that are the Miocene in age (Nabavi and Houshmandzadeh, 1984; Fig. 1b). The Late Eocene volcanic host rock is covered by the Lower Red Formation (Fig. 1b). Reuter et al. (2007) proposed that the Qom back-arc basin developed as a consequence of the Zagros collision.

2.2. Local geology

The Badroud deposit is found in the Late Eocene volcano-sedimentary rocks (Fig. 2) distributed extensively across the area and the associated gabbro dikes. Based on field investigation, they are compositionally divided into two units (Fig. 3a and b). Both units constitute barite mineralization host rock overlain by the Lower Red Formation.

2.2.1. Lower volcano-sedimentary unit

The lower unit is composed largely of a variety of altered rhyolite, rhyodacite and dacite tuffs along with interbedded sandstone and conglomerate (Fig. 3a and d). Pyroclastic tuff interbedded with sediment and the presence of the vast lateral extent of the lava flows suggests a submarine condition. This complex is characterized by variegated and contrasting colors in the rock and widely-manifested alteration (Figs. 3b and 5a). They are grayish to white in color, older in age and show a porphyritic texture consisting of phenocrysts of quartz as rounded, altered plagioclase, argillaceous K-feldspar, chloritized

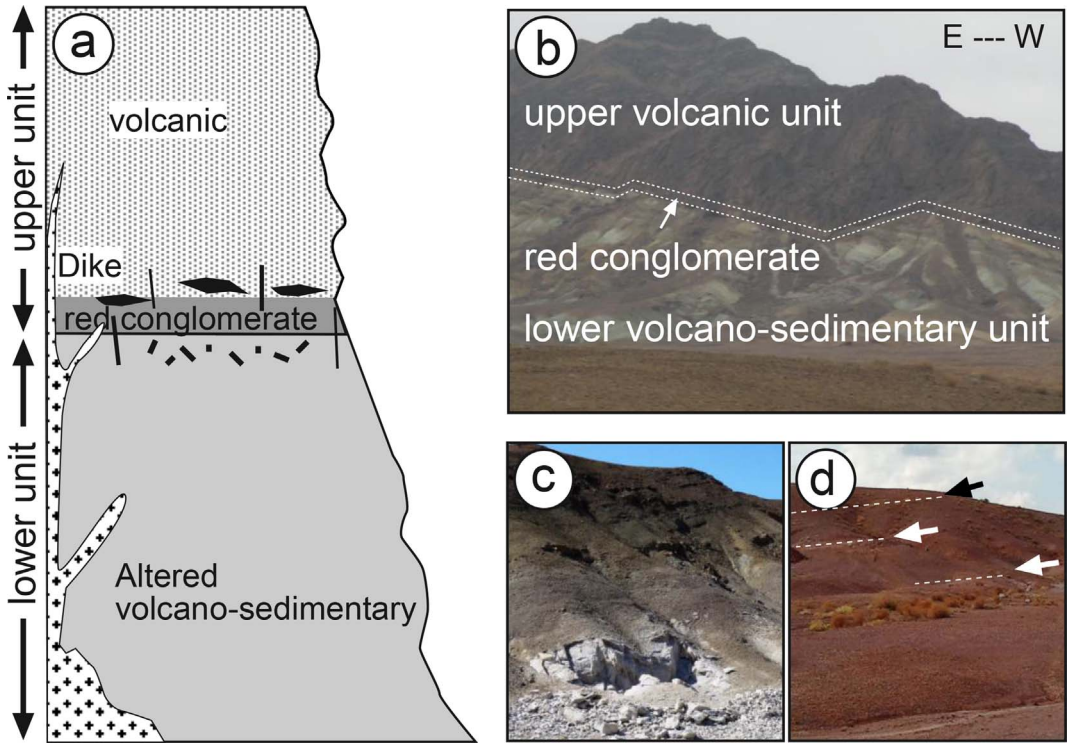

Fig. 3. (a) Stratigraphic section of the Late Eocene volcanic rocks accompanied by dikes from the Badroud deposit illustrating the position of three types of barite mineralization (Black short lines, lenses and long lines are type I, II and III, respectively). (b) Least-altered andesite (upper, dark) on the top of the volcano-sedimentary and red conglomerate in the vertical section view. (c) Difference between altered acidic volcanic of lower unit and least-altered andesite of upper unit. (d) In the upper portion of photo, altered lower unit intruded by three thin barite veins (type III).

biotite and hornblende and an aphanitic groundmass composed of quartz and feldspar.

Hematite occurs around the altered pyrite in the groundmass, although part of the rock is filled with calcite veinlets and silicified grains. The grey welded tuffs with rhyolite fragments are recrystallized and the feldspar phenocrysts have completely decomposed to clay and calcite. Remnants of the glassy rhyodacitic shards reveal a primary pyroclastic deposition. The altered volcanic rock is associated with interlayered conglomerate and lesser amounts of sandstone and has been folded to some extent.

2.2.2. Upper volcanic unit

The upper volcanic unit contains a suite of andesite, basaltic andesite and rare trachyte associated with red beds at the base as a basal conglomerate and volcanic sandstone (Figs. 2 and 3c). Numerous thick barite veins exist in the andesite. This unit is younger and characterized by black color, porphyritic texture showing plagioclase and chlorite pseudomorphs after pyroxene phenocrysts in a very fine grained to aphanetic groundmass comprising plagioclase. The visible boundary between both units is easily distinguishable by its color. In vertical section, red conglomerate and light volcanic sandstone can be observed between the altered felsic and the least-altered intermediate volcanic rock (Fig. 3b).

3. Sampling and analytical methods

Detailed petrographic studies were conducted on 72 thin polished samples of the volcanic host rock and mineral assemblages of barite. Whole rock geochemical analysis was performed on the 9 least-altered volcanic rocks (barite-hosting) and nine samples from the three barite types. Pressed powder pellets prepared from crushed samples were analyzed for major oxides (SiO_2, TiO_2, Al_2O_3, Fe_2O_3, MgO, MnO, CaO, K_2O, Na_2O and P_2O_5) by X-ray fluorescence (XRF) using a Philips PN Venus 100 minilab X-ray spectrometer at Kimiya Pazhouh Alborz Laboratory, Isfahan, Iran. Loss of ignition was determined by heating sample powders to 1100 °C. Trace elements of the least-altered volcanic rocks were determined using inductively-coupled plasma mass spectrometry (ICP-MS) at Kimiya Pazhouh Alborz Laboratory. The detection limits were 0.1% and 0.1 to 1 ppm. Bulk mineralogy of the argillic alteration and barite veins was confirmed in four samples by X-ray diffraction (XRD) using a Philips 1400 diffractometer at University of Isfahan.

Petrographic and microthermometric examination of the fluid inclusions were carried out on 12 samples at the Department of Geology, University of Isfahan. The best samples were prepared on ≤150 μm-thick double-polished wafers of euhedral to subhedral crystals with acetone-soluble glue. Primary fluid inclusions were found and measured using Linkam THMSG-600 heating–freezing stage with a TMS 94 temperature controller. Heating increments of 1 °C/min were employed for measurements below 30 °C and at 10 °C/min for up to 350 °C. The accuracy was ± 0.2 °C during freezing and ± 2 °C during heating.

4. Results

4.1. Geochemistry of country rocks

Table 1 lists the major and trace element compositions of the least-altered lower and upper units of the Late Eocene volcanic samples of the Badroud deposit. They were characterized by the contents of the following: SiO_2 (49.6–62.34%), K_2O (1.08–2.84%), Na_2O (3.1–6.95%), MgO (2.23–6.68%), CaO (2.43–6.79%) and TiO_2 (0.59–0.96%). Compositionally, these rocks are andesite, rhyodacite, minor basaltic andesite. All show high-K calc-alkaline affinity (Fig. 4a and b).

When the data was plotted on a primitive mantle-normalized diagram, the samples displayed strong enrichment in large ion lithophile elements (LILE), light rare earth elements (LREE) and heavy rare earth elements (HREE) as well as strong negative anomalies for Ba, Sr, Nb and Ti, strong positive anomalies for Rb and Pb and a weakly-positive Eu

Table 1
Representative geochemical analysis of the least-altered volcanic rocks of the Badroud deposit.

Sample	M-5	M-19	M-10	M-26	M-25	M-24	M-23	M-18	M-11
Type	Basaltic andesite	Andesite	Andesite	Andesite	Andesite	Rhyodacite	Rhyodacite	Rhyodacite	Rhyodacite
Wt. %									
SiO_2	49.60	53.48	53.59	59.58	60.32	61.07	61.20	61.38	62.34
TiO_2	0.76	0.95	0.96	0.83	0.80	0.66	0.77	0.67	0.59
Al_2O_3	15.20	14.90	14.50	18.50	16.10	15.20	16.40	15.20	15.30
Fe_2O_3	3.73	3.11	3.66	3.32	1.87	1.39	1.53	1.98	1.80
FeO	8.96	8.45	8.89	4.63	4.95	4.83	3.83	4.79	4.28
MnO	0.19	0.16	0.42	0.13	0.21	0.11	0.20	0.12	0.09
MgO	6.68	4.89	3.10	3.15	2.46	2.23	3.77	3.51	4.72
CaO	6.79	6.45	6.23	3.01	3.99	2.43	3.43	3.87	3.43
Na_2O	3.56	3.10	3.35	3.96	5.82	6.95	6.74	5.11	5.29
K_2O	2.24	2.64	2.84	1.96	2.08	2.35	1.08	2.66	1.64
P_2O_5	0.27	0.93	0.35	0.49	0.47	0.32	0.33	0.25	0.29
LOI	0.12	0.48	0.12	0.14	0.12	0.53	0.53	0.68	0.56
Total	98.10	99.49	97.83	99.70	99.19	99.63	99.81	100.07	100.12
ppm									
Cr	41.35	67.62	43	59.43	54.63	64.23	68.23	45.97	43.58
Ni	14.35	12.05	14.92	14.22	14.91	14.48	15.84	15.95	15.12
Co	18.63	15.65	19.38	27.43	28.43	29.64	26.34	20.71	19.64
V	198.6	166.82	206.54	138.4	206.33	200.35	219.16	220.8	209.32
Cu	65.34	54.89	67.95	64.74	67.88	65.91	72.11	72.64	68.87
Pb	6.95	5.84	7.23	6.89	7.22	7.01	7.67	7.73	7.33
Zn	14.35	12.05	14.92	14.22	14.91	14.48	15.84	15.95	15.12
Rb	126.4	97.4	98.4	98.8	134.7	106.4	112.4	136.7	165.4
Cs	1.84	1.55	1.91	1.82	1.91	1.86	2.03	2.05	1.94
Ba	123.8	103.99	128.75	122.66	128.62	124.89	136.62	137.64	130.49
Sr	164.8	154.91	171.39	163.28	171.21	166.25	181.86	183.22	173.7
Ga	14.36	8.34	10.58	13.64	14.92	12.11	9.34	7.89	13.64
Ta	0.86	0.82	0.73	1.65	1.48	1.84	1.65	1.68	1.24
Nb	8.73	7.33	8.79	4.97	10.3	5.87	9.73	2.68	9.4
Hf	4.15	5.98	5.34	4.01	5.48	6.69	6.79	5.67	5.69
Zr	213.4	189.4	198.7	235.8	215.8	278.4	286.4	287.4	286.7
Y	18.3	16.43	19.03	26.84	17.64	25.74	28.69	27.63	29.29
Th	7.64	6.64	7.48	6.12	8.67	7.47	5.97	8.86	8.67
La	15.4	16.34	16.27	15.48	14.37	16.47	14.79	17.39	16.48
Ce	31.8	26.75	33.11	27.64	28.64	25.64	23.18	22.48	33.56
Pr	4.46	3.24	4.37	3.17	3.24	3.42	3.27	4.56	4.42
Nd	18.6	15.63	19.09	15.48	16.48	15.34	16.87	20.41	19.35
Sm	3.24	3.56	3.48	2.57	3.46	3.56	3.47	2.98	2.98
Eu	1.3	1.32	1.07	1.64	1.43	1.54	1.56	1.64	1.09
Gd	4.65	3.31	4.84	3.48	3.89	3.65	3.37	5.17	4.9
Tb	0.86	0.69	0.46	0.45	0.42	0.43	0.46	0.52	0.86
Dy	6.02	4.64	6.41	4.94	4.98	4.23	4.45	6.64	7.34
Ho	0.67	0.85	0.76	0.64	0.76	0.84	0.65	0.65	0.83
Er	1.23	0.85	1.06	0.98	0.84	0.96	1.34	0.97	1.06
Tm	0.09	0.13	0.18	0.21	0.13	0.12	0.14	0.16	0.12
Yb	2.67	2.58	2.64	3.48	3.47	2.78	1.47	3.64	3.48
Lu	0.12	0.15	0.16	0.18	0.18	0.14	0.16	0.13	0.14
Sc	27.84	23.39	28.95	27.58	28.92	28.08	30.72	30.95	29.34
Be	1.1	0.92	1.14	1.09	1.14	1.11	1.21	1.22	1.16
Li	18.34	15.41	19.07	18.17	19.05	18.5	20.24	20.39	19.33

anomaly (Fig. 4c and d). This typifies a continental environment (Gill, 1981; Wilson, 2007). On the sample plots of the TiO_2 versus Al_2O_3 diagram of Muller and Groves (2000), the geochemical signatures of the volcanic rocks are low TiO_2, high Al_2O_3 and are derived from an arc or subduction-related basin (Fig. 4e). On the Zr/Al_2O_3 versus TiO_2/Al_2O_3 discrimination diagram from Muller et al. (1992), the samples are consistent with fields of continental arc potassic and post-collisional arc potassic rock; however, the geochemical characteristics are strongly related to a continental arc environment (Fig. 4f and g). These signatures suggest orogenic volcanism for the Late Eocene rock from the Badroud, based on tectonic framework diagrams.

Verdel (2009) also proposed extensional flare up magmatism for the Late Paleocene-Eocene volcanism in the UDMA. The results of the current study for the major and trace element analysis of the volcanic rock are very similar to previously collected regional data on the UDMA (Pourhosseini, 1981; Dilek and Sandvol, 2009). They show a high potassium content. This is consistent with a recent scenario proposed by Agard et al. (2011) for the Zagros orogenic belt in Iran. The data indicates that the volcanic rock of the Badroud belongs to a continental arc related to subduction of the Neo-Tethys (e.g., Forster et al., 1972; Berberian et al., 1982; Sengor, 1987).

4.2. Alteration

Despite the upper volcanic rock, the primary texture of Late Eocene lower volcanic rock has not been observed in the Badroud area. On the field investigations and optical microscopy observations, argillic, propylitic, silicification and hematization have been identified in the study area. Argillic alteration is rather widespread (Fig. 3b) and can be easily recognized on the field by its greyish to olive-greenish color. The texture of the Late Eocene lower volcanic rock has been completely destroyed by strong alteration. XRD analysis and optical microscopy studies indicate that the argillic alteration is mostly composed of montmorillonite, kaolinite and minor illite with traces of quartz as

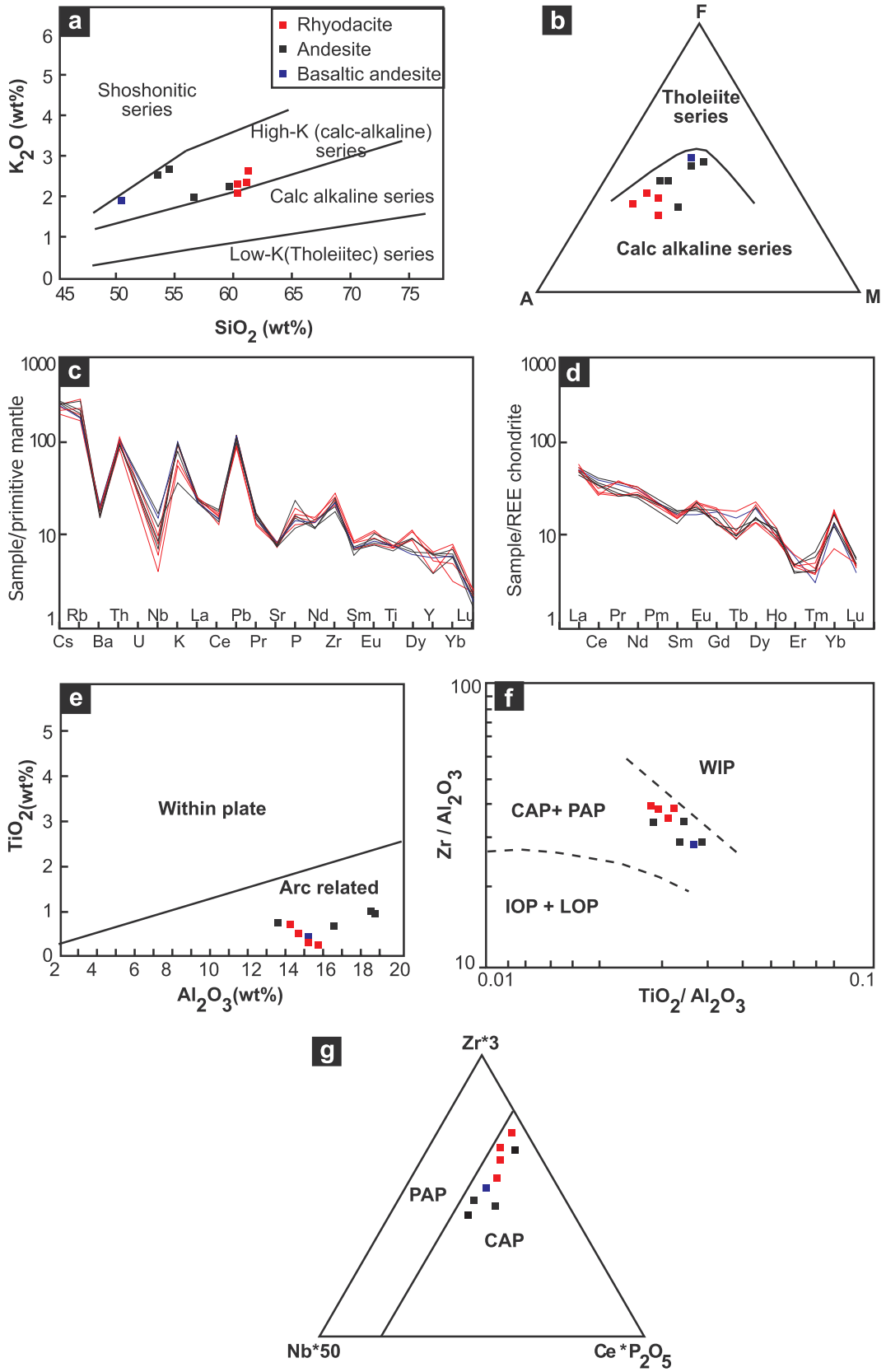

Fig. 4. Plot of least-altered samples from the Badroud deposit in petrology diagrams. (a) K_2O vs. SiO_2 diagram of Peccerillo and Taylor (1976). Most samples belong to high-K calc-alkaline series. (b) AFM diagram of volcanics (Irvine and Baragar, 1971) showing they grouped into the calc-alkaline field. (c) Extended trace-element diagram of whole rock samples. Data are normalized to primitive mantle using McDonough and Sun (1995) (d) REE pattern of volcanics normalized using Boynton (1984); they are enriched in light REE. (e) Plot of the volcanic rocks in TiO_2 vs. Al_2O_3 diagram of Muller and Groves (2000) is proposed the arc-related. (f) The Zr/Al_2O_3 vs. TiO_2/Al_2O_3 diagram shows the calc-alkaline series, consistent with products of a continental arc and post arc, compressional environment (Muller et al., 1992). (g) Plot of the samples in ternary diagram of Muller et al. (1992) falling in the CAP field. Abbreviations in (f) and (g): CAP, continental arc potassic rocks; PAP, post-collisional arc potassic rocks; IOP, initial oceanic arc potassic rocks; LOP, late oceanic arc potassic rocks.

cristobalite, feldspar, zeolite and carbonates. This alteration is known as bentonite (Fig. 3c); however, the presence of kaolinite in the vicinity of the barite most likely resulted from the interaction between hydrothermal fluid and the felsic hosted (Yeats et al., 2017) by the lower unit. This process can produce acidic hydrothermal fluid.

Silicification forms as very fine or medium grained quartz in veinlets associated with barite veins. In some areas, red jasper occurs as a replacement of the original texture of the host rock near barite lenses and also wood opal by chalcedony. The broad extent of propylitic alteration consists of epidote, Fe-chlorite, calcite and quartz followed by phenocrysts of pyroxene and plagioclase and groundmass. Hematization occurs at higher oxygen fugacity and displays a red color. It contains hematite, calcite, chlorite and clay minerals. Abundant hematization is observed near the disseminated barite; thus, based on geological observations and paragenetic characteristics, precipitation of barite I and II is dominated by hematization. This close relationship suggests mixing between hydrothermal fluid and seawater (Baioumy et al., 2013).

4.3. Mineralization

The main barite mineralization is located in the western portion of the Badroud area in a NW-SE direction (Fig. 2). As noted previously, barite mineralization occurs as lense, disseminated or vein types as well as rare breccias in the Late Eocene volcanic rocks (Fig. 2). They were formed in a continuous period during the Late Eocene. The mineralization extends NW-SE and has a total length of about 3 km (Fig. 2). It includes more than 23 barite lensoid veins. On the basis of the structure and textural observations of the veins, grain size and shape of the barite crystals, three distinct types of barites were recognized from the Badroud deposit, types I, II and III, that respectively range in age from oldest to youngest (Table 2). Each style displays specific properties with different morphologies. The paragenetic sequence of the Badroud barite indicates three types of mineralization related to baritization events (Figs. 5 and 6).

4.3.1. Barite I

Type I barite formed earlier than types II and III in the Late Eocene altered volcano-sedimentary rock of the lower unit along the 2.5 m-thick NW-trending fault zone (Fig. 5b and c). The veinlets are almost pure barite with a simple texture. There is a close relationship between this phase of barite and argillic and hematization alterations. The alignment of the barite outcrop displays localization trending NW-SE and controlled by fractures in the crushed zone.

This group presents as networks of pods consisting of decimeter-scale lenticular bodies, radial crystal clusters in the surrounding volcanic debris (Fig. 5b), disseminated and discontinuous barite that is white to pinkish in color and large (cm-sized) euhedral tabular and bladed crystals (Fig. 6a and b). XRD analysis indicates that the carbonate and sulfate phases associated with barite are calcite and gypsum, respectively. The barite is intergrown with minor abundant coarse-grained calcite. Jasper appears late and fills the open space between the barite and calcite minerals.

Table 2
Comparison of the characteristics of the barite mineralization of the Badroud deposit.

Type	Host rock	Structure	Morphology of crystal	Gangue	Sulfides
Brt I	lower unit	networks of veinlets	bladed and euhedral large tabular	Cal, Gp, Fl	–
Brt II	upper unit	lensoid massives	medium to fine-grained tabular	Silica	Py, Ccp
Brt III	lower and upper units	thin veins	acicular	Qz	Py, Gn, Stbn, Sbr

4.3.2. Barite II

Type II barite occurs as several subparallel lensoid veins in the upper unit of the Late Eocene rock and covers a much larger area in the host rock than does type I (Fig. 5d). These wide lenses can be traced for a maximum of 50 m long, strike approximately N-S and have a true width of 2–4 m (Fig. 5d). In-hand specimens a simple mineralogy with barite and minor silica is observed. This style was observed as being subhedral medium-to fine-grained tabular white to grey color crystals of massive barite with less than 4 mm in grain diameter (Fig. 6c). Barite veins are associated with silica-filled tension cracks including red jasper (Fig. 5f) with a fine granular texture, polygonal grains of quartz and other silica gangue minerals resembling to chalcedony and opal. A sulfide phase has not been identified in-hand specimens so far. Mineralography has revealed the presence of this phase as an accessory mineral. The sulfides as pyrite and chalcopyrite, are finely disseminated.

4.3.3. Barite III

This group formed late in the paragenesis after barite types I and II (Fig. 7). Type III is marked by thin veins (Fig. 5e) along steeply dipping fractures (80–90°) with relatively fine-grained, acicular crystals of barite (Fig. 6c). The veins are white to reddish in color throughout both units of the Late Eocene volcanic rocks. Barite veins with at least 100 m in length appear along the strike of the outcrop with an average thickness of 0.1 m (Fig. 5e). The veins commonly trend NW-SE. The mineral assemblage is dominated by minor galena, pyrite, stibnite and cinnabar. Acicular crystals of barite and fine-grained elongated sulfide minerals appear to belong to a unique paragenetic stage (See Fig. 7). In addition, several short veins have a brecciated texture (Fig. 6d) with large fragments of barite I and pyrite crystals occurring in a reddish matrix of silica and hematite (that resembles jasper) about 1 m in thickness in the lower unit. Malachite, covellite and calcite are products of weathering and oxidized mineralization.

XRD analysis of the barite samples showed that the associated minerals were mostly composed of barite, quartz and small amount of calcite, gypsum, fluorite and sulfide minerals in some samples. In addition to these minerals, malachite and secondary Fe oxides were commonly observed in thin sections. All barite samples of the Badroud area used for chemical analysis primarily consist of > 90% purity with a specific gravity of ≥ 4.1.

The distribution of major oxides in the different barite types is shown in Table 3. With the exception of BaO and SiO_2 contents that range from 79.81% to 92.03% (wt.) and 0.67% to 10.79% (wt.), respectively, barite samples exhibited low concentrations of major oxides such as Al_2O_3 (0.33–1.94% wt.), Na_2O (1.25–1.43% wt.), K_2O (0.12–0.41% wt.), TiO_2 (0.20–0.24% wt.) and CaO (0.02–1.6% wt.). MgO, MnO and P_2O_5 occurred in very low concentrations of less than 0.1% (wt.). The Sr distribution changed as the Ba content increased and there was a positive correlation between them ($R^2 = 0.61$) that is similar to other arc-system seafloor deposits (Hannington et al., 2005). The Sr/Ba ratio in all samples studied was below 0.5.

4.4. Structural control

Primary regional geological studies and satellite images in combination with field observation have shown that the Kashan barite deposits are structurally distributed between two important faults trending NW-SE and NE-SW (Fig. 1c). On a regional scale, the first group comprises major map-scale faults (Kashan and Kuh-e Dom) that are mainly of the thrust and dextral strike-slip type (Fig. 1c). These structural elements extend parallel to the Zagros thrust fault and may have formed or reactivated during convergence of the Arabian and Eurasian plates (Nadimi and Konon, 2012; Kananian et al., 2014). The calc-alkaline volcanic activity of the UDMA began with this compressional tectonic. The minor and local faults (second group trending NE-

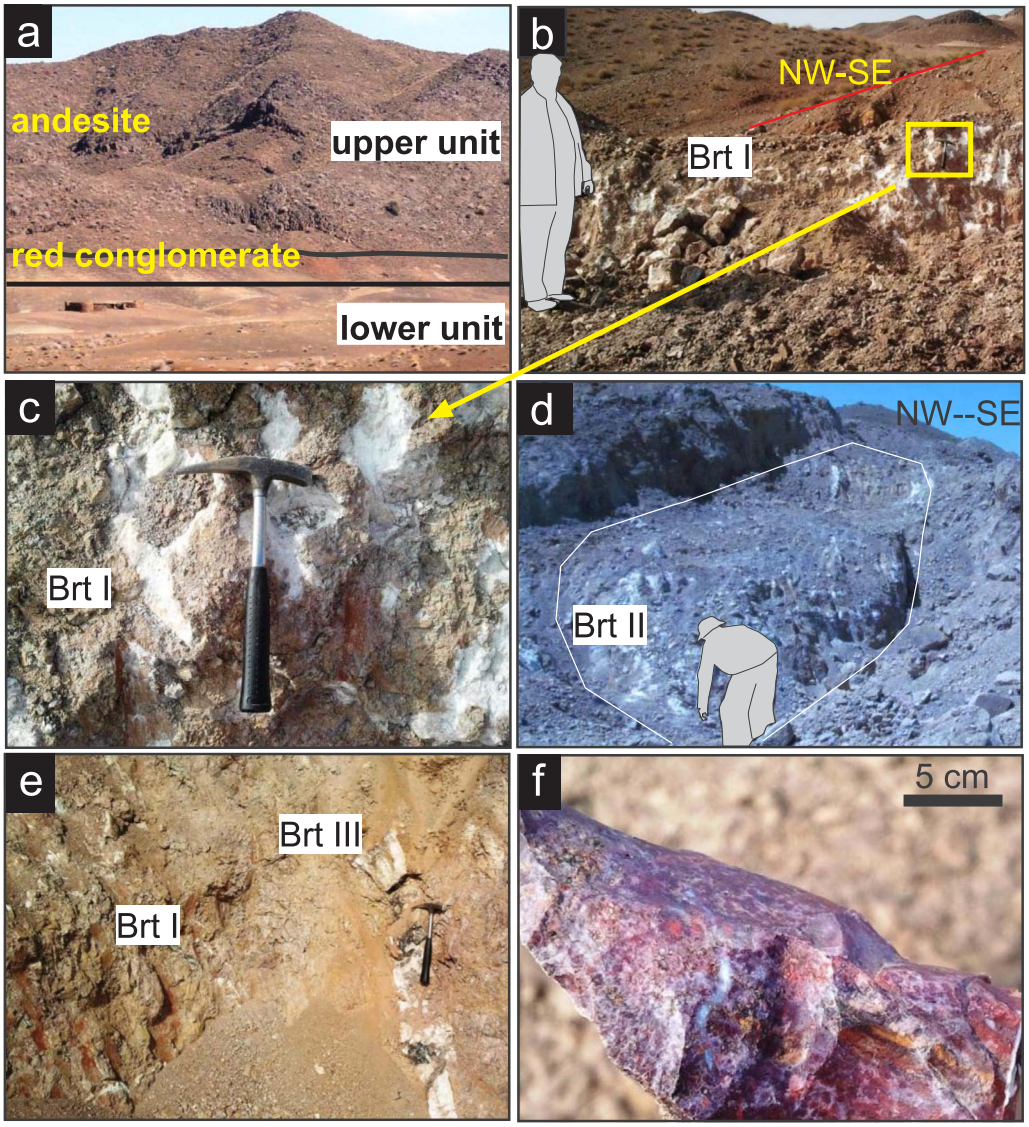

Fig. 5. Field photographs of volcanic rocks and different types of barite mineralization from the Badroud deposit. (a) Outcrop of the red conglomerate between upper and lower volcanic units. Building for scale in altered lower unit. (b) Lenticular and bending cracks filled by white coarse barite crystals (type I) within a NW-SE trending fault zone. Locally, lower volcanic rocks are hematized. (c) Close-up view of the radiating barite I aggregate. Hematization envelop crosscut by barite filling. Core of barite pockets is comprised of volcanic material. (d) Outcrop of the lensoid vein of barite (type II). This wide lens consists of white massive barite and minor silica. (e) The view is from the two types of barite, note the characteristically sharp contact between the barite I and III. (f) Close-up view of the red iron silica. See the text for explanation.

SW) are normal and sinistral strike-slip faults (Nadimi and Konon, 2012).

The second group formed in association with extensional fissures. Verdel et al. (2011) suggested that the branches of these faults have E-W and N-S directions. On a regional scale, the locations of the east Kashan barite deposits from four sites (Fig. 1b) are bordered by NW-SE-trending faults. It is likely that both the fault systems provided vertically important channels for ore-forming fluids in the study area, although the first group of faults occurred before barite mineralization. Despite the morphology of barites I and II as disseminated and lens, respectively, mineralization in the Badroud deposit probably formed in syn-volcanic crushed zones with maximum lengths of 3 km (Fig. 2) parallel to the NW-SE-trending fault zone (Figs. 5b, 8a and c).

Based on the field data, the earliest mineralization developed in the presence of the network of lens-shaped occurrences of type I barite parallel to the NW-SE-trending fault zone. Lateral movement in this fault zone is clear. Based on structural evidence in field of the right lateral motion in the argillic alteration before formation of types II and III barite veins with less than several decimeters in displacement, it can be proposed that the behavior of the faults for that period was NW-SE dextral strike-slip in style. Type II barite is more likely to form in an extensional stress regime. Type III barite occurred along the fault zone with a NW-SE trend (Figs. 5e, 8a and c). The orientation of dikes and faults is also approximately NW-SE (Fig. 8a and b) in the Badroud area.

4.5. Fluid inclusions

Fluid inclusion studies were carried out on 12 samples from the different mineralization stages (I, II and III). About 124 inclusions were measured for homogenization temperature (Th) and 94 salinity determinations were obtained. The data for all inclusions are summarized in Table 4 and Fig. 10a and b. Nearly all fluid inclusions observed were small in size (3–25 μm) (Fig. 9a, b and c). Their shapes varied from commonly irregular, spindle, tubular to rare angular. At ambient temperatures, most primary inclusions were typically two-phase (liquid (L) and vapor (V) for which V occupied < 15% of the inclusion volume) and were 8–20 μm in size (Fig. 9a, b and c). V bubbles in two phase (L + V) fluid inclusions from barite I occupied 20% to 25% (vol.) of

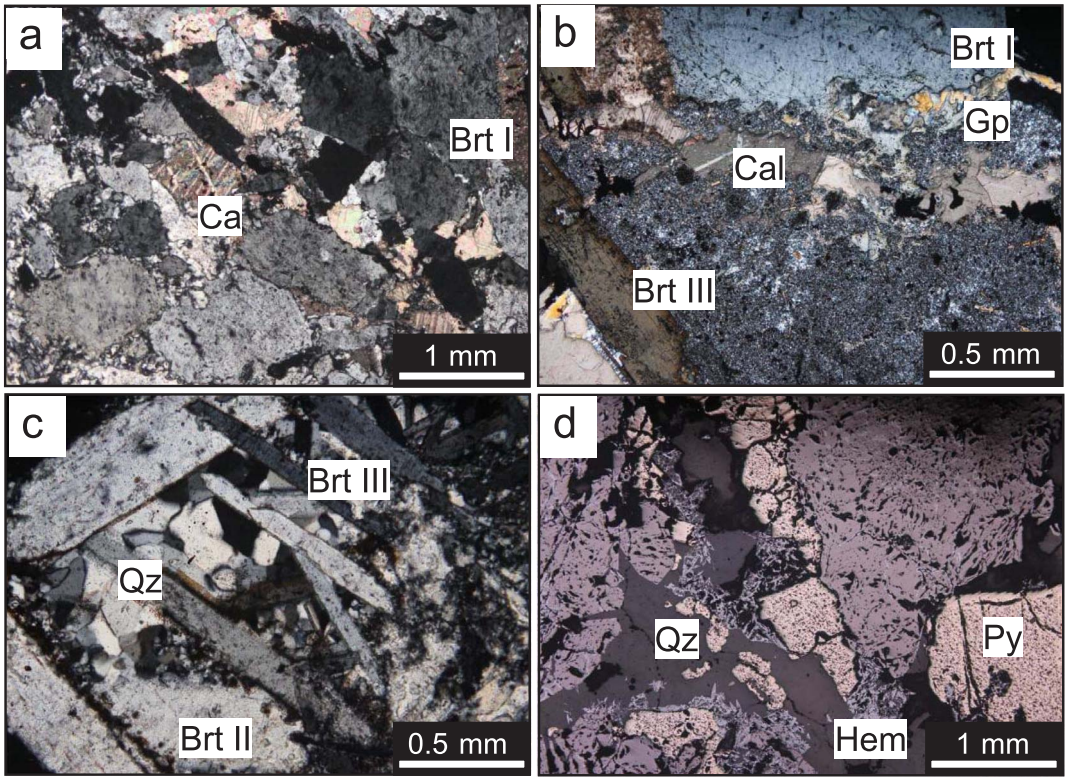

Fig. 6. Photomicrographs showing petrography and textural characteristics of barite samples collected from various shapes and sizes from the Badroud barite deposit. All photomicrographs are transmitted cross-polarized light except d. (a) Pore space of large well-formed barite I crystals is filled by calcite crystals. This texture occurs extensively through the lower unit. The quartz mineral is paragenetically filled the border of barite I and calcite minerals. (b) Two growth stages of precipitation barite indicate depositional conditions. Large bladed barite I intergrown with coarse grained calcite. Jasper invaded the barite I and calcite and dissolved their edges which locally is cut by barite III crystal. Note a little sulfide (chalcopyrite, pyrite) adjacent calcite. (c) Growth of the randomly-oriented, acicular barite III crystals in center and tabular barite II replaced by quartz at the down. Replacement of very fine quartz (jasper) by polygonal grained quartz and opal by chalcedony (lower part). Barite III has the distinct contact with polygonal grained quartz and an obscure margin with jasper. (d) Breccia sample with fragments of pyrite in the hematite-silica matrix in reflected light. Mineral abbreviations used in Fig. 6 and Table 2 (according to Whitney and Evans, 2010): Brt I—barite I, Brt II—barite II, Brt III—barite III, Cal—calcite, Ccp—chalcopyrite, Fl—fluorite, Gn—galena, Gp—gypsum, Hem—hematite, Py—pyrite, Qz—quartz.

inclusions (Fig. 9a).

V-rich fluid inclusions were observed in most samples. Single phase (L) inclusions were also observed in the samples. Two-phase (L + V) L-rich inclusions may have become trapped in fractures or confined to the growth zones of barite crystals (Fig. 9b). Careful microscopic study of crystal shape and size distribution indicates three types of barite (Fig. 9a, b and c). The results of microthermometry measurements show the homogenization temperatures of 160–338 °C for L + V into L for primary fluid inclusions in barite (Fig. 10a). The last ice-melting temperatures (T_{Lm}) were −0.8 to −15.5 °C. Salinity from the last ice-melting temperatures was calculated (FIA of Goldstein and Reynolds, 1994) to be 1.40% to 19.0% (wt.) NaCl eq. (Fig. 10b).

Plots of salinity versus homogenization temperature for all fluid inclusions indicate that they can be classified into three clusters (types I, II and III) (Fig. 11). Type I inclusions (Fig. 9a) suggest that they were all of a high temperature fluid; however, type II inclusions occurred with less salinity. The resulting fluid for barite III strongly differed from those of barites I and II. The plots of moderately saline hot fluids of barite I in Fig. 11 show an overall decrease in salinity and a linear distribution, probably concomitant with dilution. The fluid of barite II points to mixing and of barite III is associated with an increase in density from type II to type III. On Wilkinson's diagram (2001) fluid inclusions from barite I plotted in epithermal field. According to this diagram barite II and III belong to Kuroko- and Irish-type fields, respectively (Fig. 11).

5. Discussion

5.1. Interpretation of barite characteristics

Mineralogical features, textural relationships and morphological investigations revealed three distinctive styles of barite mineralization at the Badroud deposit. The early phase was stockworks of euhedral bladed and large tabular barite as sulfide-barren stage I. The later phase was lensoid and thin veins of medium to fine tabular barites denoted as sulfide-bearing stages II and III (Table 2). The presence of acicular barite with randomly-oriented finely acicular sulfide minerals in barite III were related to an increase in saturation by fluid (Jamieson et al., 2016). The early phase includes pure barite plus minor calcite, gypsum and late silica without a sulfide phase. The later epoch comprises barite plus silica with minor sulfide (see paragenetic diagram in Fig. 7). In comparison with the sulfide-barren phase, the sulfide-bearing phase of barite lacks of calcite and the presence of silica.

The scarcity of calcite suggests that CO_3^{2-} was absent as a minor complexing agent (Margoum et al., 2015) and the silica as chalcedony, opal and quartz points to a decrease in pH in the hydrothermal fluid. Recrystallization of amorphous silica to polygonal grain quartz occurs throughout the vein formation. The major and trace elements signature of the barite shows from the somewhat low Sr, K and Ca that these samples did not form in a deep marine environment. The lower Sr/Ba ratio of barite is also a good indicator (Table 3) of formation at shallow depths, similar to exhalative systems (Jamieson et al., 2016; Lode et al., 2016). The minor variations in the Ba, Rb, and Sr contents and Rb/Sr ratio are probably controlled by differences in the temperature of formation (Hanor, 2000) and mineralogical composition.

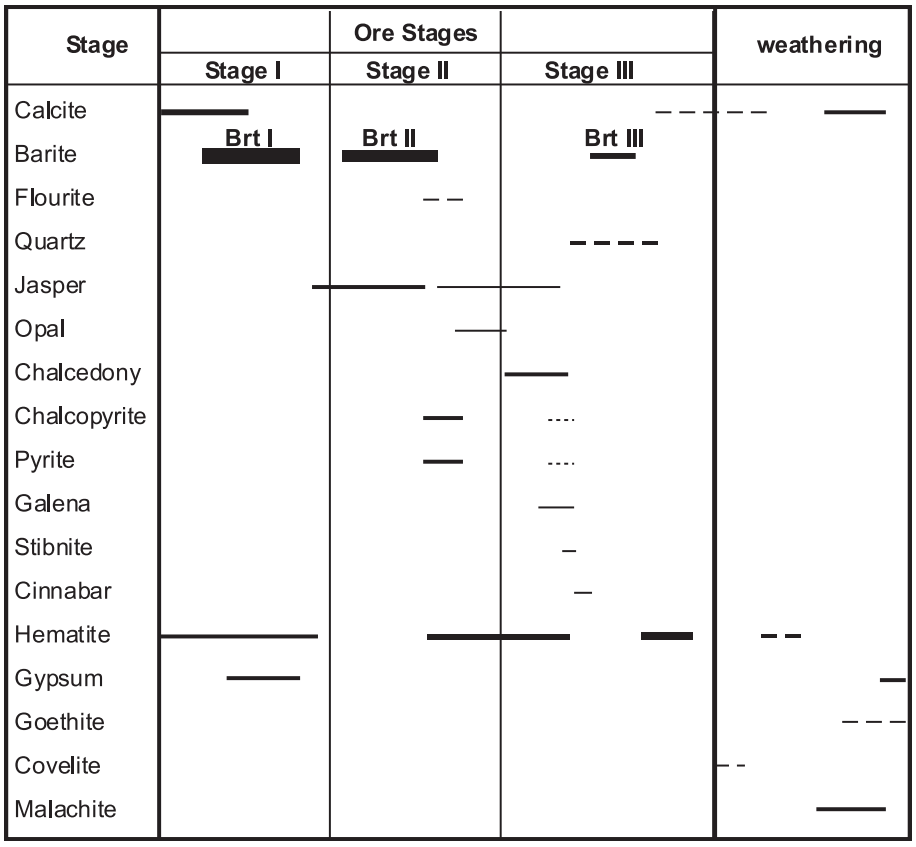

Fig. 7. Summary of paragenetic diagram in the Badroud deposit.

Table 3
Chemical composition of barite samples of the Badroud deposit.

Sample	B-37	B-38	B-39	B-40	B-41	B-42	B-43	B-44	B-45
Wt. %									
SiO_2	0.67	1.92	2.07	1.42	5.22	7.13	5.83	9.79	9.07
TiO_2	0.23	0.22	0.22	0.23	0.24	0.21	0.20	0.2	0.21
Al_2O_3	0.61	1.04	0.70	0.52	0.53	1.45	1.66	1.94	0.33
Fe_2O_3	0.04	0.06	0.05	0.02	0.02	0.50	0.46	0.31	0.02
FeO	0.25	0.39	0.36	0.10	0.14	3.26	3.05	2.03	0.15
MnO	0.06	0.03	0.08	0.03	0.01	0.01	0.09	0.02	0.09
MgO	0.08	0.04	0.06	0.04	0.04	0.04	0.04	0.07	0.04
CaO	1.19	0.40	1.56	0.24	0.15	0.02	0.03	1.46	0.79
Na_2O	1.37	1.32	1.26	1.37	1.43	1.04	1.27	1.29	1.25
K_2O	0.12	0.20	0.17	0.13	0.14	0.23	0.34	0.41	0.12
P_2O_5	0.02	0.02	0.02	0.02	0.03	0.02	0.02	0.02	0.02
L.O.I	0.83	0.63	1.08	0.45	0.83	1.40	1.05	1.19	1.53
BaO	69.63	68.81	68.10	70.20	67.33	62.23	62.93	60.48	64.00
SrO	2.58	2.58	2.65	2.53	2.04	2.19	2.46	2.03	1.71
SO_3	21.85	21.87	21.10	21.83	21.12	19.40	19.68	19.34	20.14
Total	99.53	99.53	99.48	99.13	99.27	99.13	99.11	100.58	99.47

Table 4
Summary of the homogenization temperatures and salinities for fluid inclusions of the Badroud deposit.

Stage	$T_{Fm\ ice}$ (°C)		$T_{Lm\ ice}$ (°C)		$Th_{(°C)}$		Salinity (%)	Type of barite
	N	Rang	N	Rang	N	Rang		
I	34	−39.5 to −45	51	−5.3 to −9.5	61	256 to 338	8.3 to 13.4	barite I
II	16	−22 to −40	27	−0.8 to −6.0	39	160 to 214	1.4 to 9.2	barite II
III	7	−35 to −39	16	−10.3 to −15.5	24	166 to 212	14.3 to 19.0	barite III

Abbreviations: N = number of inclusions analyzed, $T_{Fm\ ice}$ = First melting ice temperature, $T_{Lm\ ice}$ = Last melting ice temperature, Th = homogenization temperature.

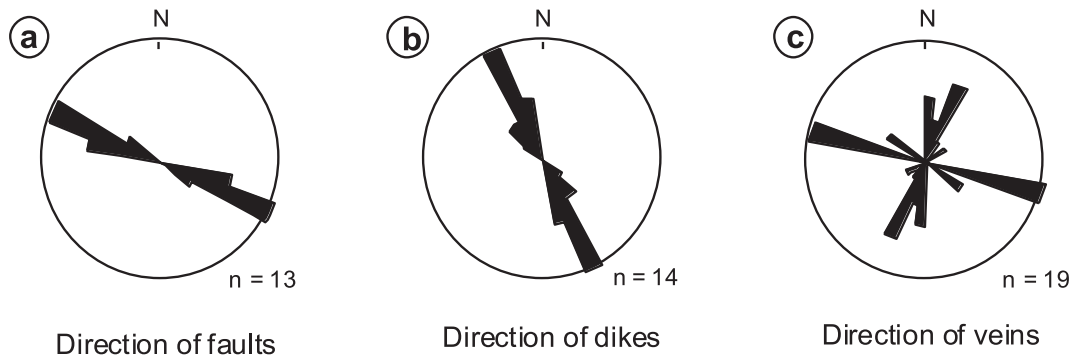

Fig. 8. Orientation of structural data from: (a) faults, (b) dikes and (c) barite veins obtained the Badroud deposit. (c) Note to multiple trend of veins compared to faults and dikes.

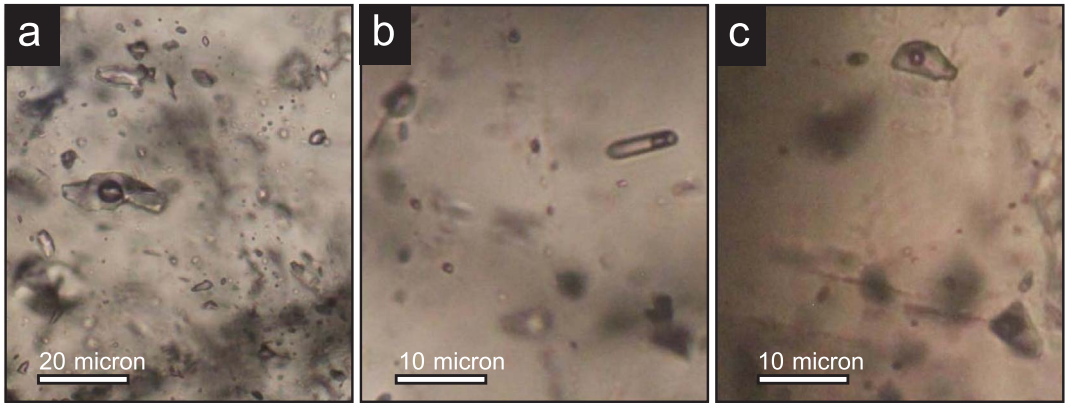

Fig. 9. (a) Coexisting two-phase liquid rich- and single phase inclusions. Irregular primary fluid inclusion (center) in barite I. (b) Tabular primary fluid inclusion in barite II. (c) Spindle-like primary fluid inclusion in barite III.

As described above, fluid inclusion produced important new data concerning the origin of the Badroud barite mineralization. Interestingly, there are significant differences between the first stage (sulfide barren) and the second and third stages (sulfide bearing) of barite formation due to the high homogenization temperature of stage I and moderate homogenization temperature of stages II and III (Fig. 11). Microthermometry results suggest that barite I experienced hydrothermal activity associated with the involvement of faintly magmatic fluids trapped at deeper levels. The second type of inclusion with the low salinity of stage II is consistent with a dilution event with seawater. During the migration of fluids, extensive chemical interaction and mixing produced saline fluid III.

5.2. Hydrothermal fluid evolution in relation to volcanic events

5.2.1. Barite I in lower volcano-sedimentary unit

Field observasions in the Badroud area shows that andesitic-dacitic flows associated with extensive the rhyolite rock of the lower unit are indicative of a bimodal-felsic environment. The morphology of barite shows that deposition may have occurred during development of the lower unit or immediately after its replacement. More detailed evalution of the barite formation was obtained by examination of the host rock. New data from the chemistry of the least-altered volcanic samples of the Late Eocene units in the Badroud area indicate high-K calc-alkalin orogenic volcanism.

Note that the magmatic activity related to the post-collisional regime released metal-poor magmatic fluids from volatile-rich felsic magma (Huston et al., 2011). Previous studies show that the most important barite-rich seafloor massive sulfides were associated with mafic to felsic volcanic rock (Shadlun et al., 1991; Davis et al., 2003; Melekestseva et al., 2014). Barite I is dispersed in a network of lens-shaped barite or veinlet stockworks (Fig. 12a) along a NW-SE-trending fault zone. It was found that barite I as a stockwork can form in a stringer zone. In the core of this stringer, exists breccia (Fig. 12a) containing barite-rich clasts within a silicic and hematite matrix. The barite and pyrite clasts are rounded to subangular with less than 10 cm in size (average 1–4 cm). Stringers of barite stockworks as feeder channelways are common in volcanic massive sulfide (VMS) environments (Melekestseva et al., 2014). There is clearly a genetic association between barite I and the alteration zones at the top of the lower unit.

The argillisation and silisification associated with barite I increasingly seem to form in an acidic hydrothermal system. As discussed above, the highest homogenization temperature value of barite I reflects its deposition from hydrothermal fluid (Fig. 11). In other words, extensive outbreaks in volcanic activity associated with barite I would have created the necessary heat from the magma reservoir to circulate hydrothermal fluid through the hot rhyolite and rhyodacite rock from the lower unit in the order of a few millions years (Von Quadt et al., 2011). It is nonetheless significant that the homogenization temperature of inclusions of barite I versus salinity indicates a linear distribution pattern resulting from fluid dilution during the waning of the hydrothermal system as (Fe, Ba)-rich fluids ascended along faults and fractures in contact with seawater and decreased the temperature from 338 to 256 °C and increased the fO_2. In the Badroud area, such a scenario suggests that barite I was linked with submarine magmatic-hydrothermal activity similar to the accepted magmatic-hydrothermal model for Kuroko-type deposits (e.g., Urabe, 1987; Large et al., 2001).

5.2.2. Barite II and III in upper volcanic unit

Geochemical studies indicate that the Late Eocene rock comprising orogenic andesite accommodates red conglomerate at the basement. The deposition of the red conglomerates at the basement represents the earliest signature of the onset of post-collision tectonic activity that ultimately resulted in the formation of orogenic volcanic rock. The nearest igneous intrusions, gabbro dikes (Fig. 12c) in the southern part of the study area, intruded the Late Eocene volcanic rock (Fig. 2),

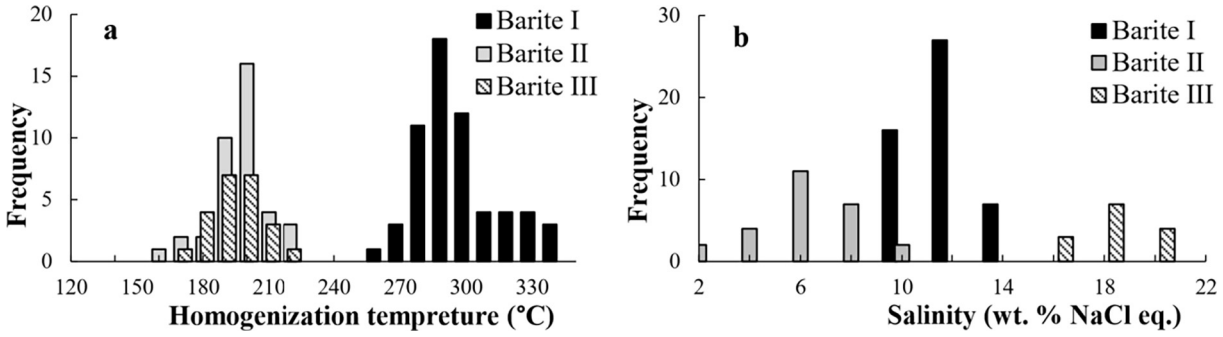

Fig. 10. Histogram of homogenization temperature and salinity for barite in the Badroud deposit.

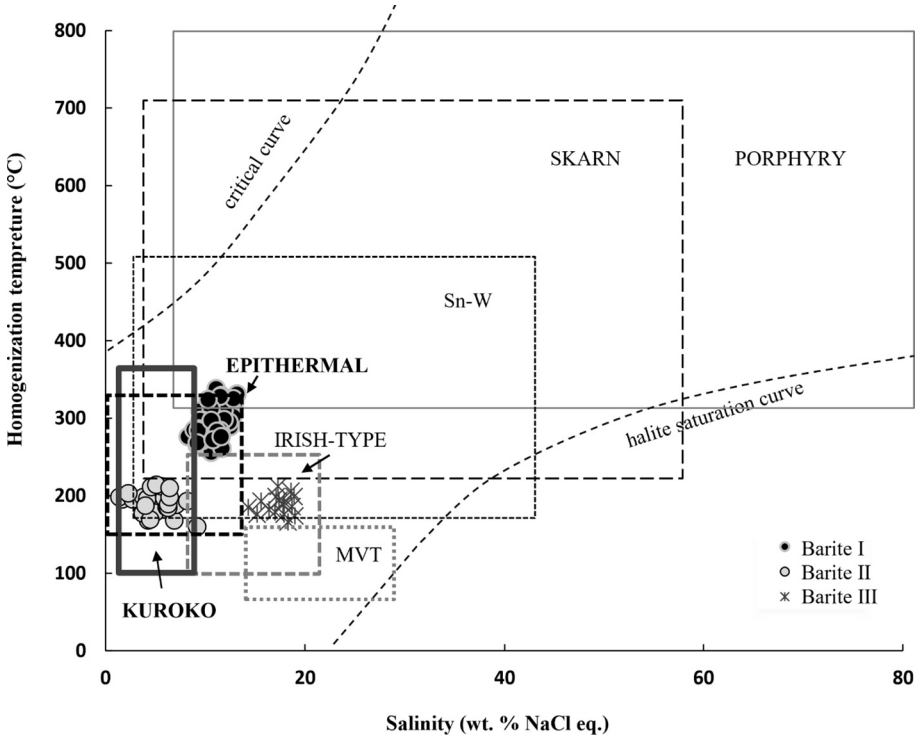

Fig. 11. Final homogenization temperature (Th) vs. salinity of fluid inclusions in different barite types from Badroud deposit. Th–salinity diagram showing typical ranges for inclusions from different deposit types (Wilkinson, 2001).

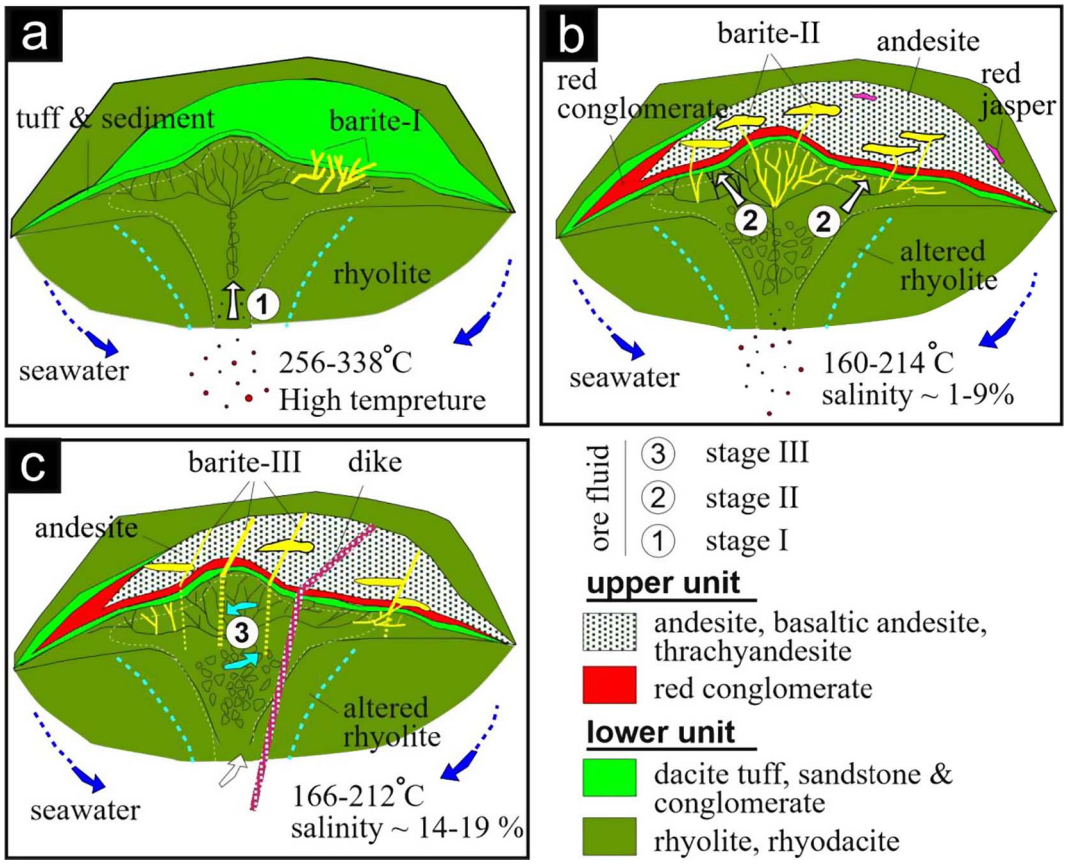

Fig. 12. Proposed schematic model for barite formation at stages I, II and III in the Badroud deposit (after Herzig and Hannington (1995) with additions and modifications). Comparison of this model with different types of barite in Fig. 5. (a) Stockworks of barite I form during/after fault in crushed zone at stage I. (b) Wide lenses of barite II cross cutting barite I at stage II. (c) Thin veins of barite III cross cutting barite I and barite II at stage III.

although most of the VMS deposits are also cut by gabbroic dikes (Fershtater et al., 2007; Tessalina et al., 2017).

Lensoid veins of barite II (Fig. 12b) are shorter in length and thicker in width. The presence of negligible barite III veins shows that they were emplaced later than the barite II in the orogenic andesite rock (Fig. 12c). As revealed by the microtermometric data, fluid inclusions from stage II (Table 4) are described as moderate temperature-low saline inclusions, while the third type of inclusions with higher salinity in stage III are consistent with saline water. According to studies conducted by Wilkinson (2001), saline barite III can be attributed to the mixing of meteoric and hydrothermal fluids (Fig. 12c) that probably occurred at the basement–cover interface unconformity as red conglomerate. Subsequently, barite III also probably formed at shallower depths than barite I and II.

5.3. Implications for barite exploration

This study identified the altered Late Eocene rock rocks associated with barite mineralization that could be used as an inexpensive indicator for barite exploration in a regional scale. The extensive hydrothermal alterations offer more exploration targets for barite I around the Badroud area. Field investigations show that strike slip faults trending NW-SW in the Late Eocene bimodal volcanic rocks are also important control for barite mineralization. To explore more barite occurrences in this area, it should be focused beneath and on top of the red conglomerates of the upper unit in particular for barite I and II, respectively. The characteristics and similarities of the Badroud barite deposit to the Kuroko-type deposits make it possible to identify similar mineralization along the Qom-Kashan belt that has been remained unknown due to the lack of systematic exploration.

6. Conclusion

The results of field investigation and identification of chemical characteristics of host volcanics associated with the morphology and chemistry of barite, the mineralogy of the vein as well as microthermometry data have provided a new approach for predicting the probable mechanism of barite mineralization in the Badroud area. The Badroud barite deposit shows three types of mineralization: (1) stringer zones of barite I as stockworks and breccia (Fig. 12a); (2) massives of barite II as lenses (Fig. 12b) locally dominated by red silica and a minor amount of fine-grained sulfides; and (3) thin veins of barite III (Fig. 12c) with small amounts of sulfide and silica.

As stated, the Badroud barite is related to the Late Eocene bimodal-felsic rock that formed in a shallow continental basin. It is suggested that the barite precipitation was produced from the dilution and mixture of at least two components, hydrothermal fluid and seawater. The subsequent interaction of heated seawater or meteoric water with the upper unit caused formation of negligible barite veins and abundant red amorphous silica from the saline fluid. The nature of the mineralization and alteration assemblages of the Badroud barite deposit is significantly similar to those observed in Kuroko-type VMS deposits in an arc setting.

Based on geological and geochemical features and fluid inclusion studies in the Badroud area, the magmatic-hydrothermal model without base-metal sulfides (barren barite deposits) suggests the formation of barite I at high temperatures (> 300 °C). The trend in Fig. 11 for barite I is likely diluted with seawater or meteoric water. This event suggests that the barite II phase mineralization formed with the cooling and further dilution of end member hydrothermal fluid in a submarine condition. During their migration, as presented some contact relations, fluids from the host rock (volcanic rock and conglomerate) experienced extensive chemical interaction which led to the formation of barite III from saline fluid.

Acknowledgments

We would like to thank the Department of Geology at the University of Isfahan for allowing the use of their laboratory facilities. The authors are gratefully appreciated Dr. Nadimi, Dr. Jazi and Dr. Khalili for helpful suggestions and H. Jafari for help in sampling. The authors also are thankful to Prof. F. Pirajno, Head Editor, Dr. H. Asadi Haroni, Associate Editor, and the anonymous reviewers for the valuable review and instructive comments (geologic and nongeologic).

References

Agard, P., Omrani, J., Jolivet, L., Whitechurch, H., Vrielynck, B., Spakman, W., Monie, P., Meyer, B., Wortel, R., 2011. Zagros orogeny: a subduction-dominated process. Geol. Mag. 148, 692–725.
Aghanabati, A., 1986. Geological Map of Iran, Scale 1:10000000. Geological Survey of Iran, Tehran.
Alavi, M., 1996. Tectonostratigraphic synthesis and structural style of the Alborz Mountain system in northern Iran. J. Geodyn. 21, 1–33.
Alavi, M., 2004. Regional stratigraphy of the Zagros folded-thrust belt of Iran and its proforeland evolution. Am. J. Sci. 304, 1–20.
Amidi, S.M., Zahedi, M., 1975. Geological Map of Kashan, Scale 1:250000. Geological Survey of Iran, No F7, Tehran, Iran.
Azizi, H., Tanaka, T., Asahara, Y., Chung, S.L., Zarrinkoub, M.H., 2011. Discrimination of the age and tectonic setting for magmatic rocks along the Zagros thrust zone, northwest Iran, using the zircon U-Pb age and Sr–Nd isotopes. J. Geodyn. 52, 304–320.
Baioumy, H.M., Khedr, M.Z., Ahmed, A.H., 2013. Mineralogy, geochemistry and origin of Mn in the high-Mn iron ores, Bahariya Oasis, Egypt. Ore Geol. Rev. 53, 63–76.
Berberian, F., Muir, I.D., Pankhurst, R.J., Berberian, M., 1982. Late Cretaceous and Early Miocene Andean type plutonic activity in northern Makran and Central Iran. J. Geol. Soc. London 139, 605–614.
Berberian, M., King, G.C.P., 1981. Towards a paleogeography and tectonic evolution of Iran. Can. J. Earth Sci. 18, 210–265.
Boynton, W.V., 1984. Cosmochemistry of the rare earth elements, meteorite studies. In: Henderson, P. (Ed.), Rare Earth Element Geochemistry, Developments in Geochemistry. Elsevier, Amsterdam, pp. 63–114.
Chiu, H.Y., Chung, S.L., Zarrinkoub, M.H., Mohammadi, S.S., Khatib, M.M., Iizuka, Y., 2013. Zircon U-Pb age constraints from Iran on the magmatic evolution related to Neotethyan subduction and Zagros orogeny. Lithos 162–163, 70–87.
Davis, A.S., Clague, D.A., Zierenberg, R.A., Wheat, C.G., Cousens, B.L., 2003. Sulfide formation related to changes in the hydrothermal system on Loihi seamount, Hawai'i, following the seismic event in 1996. Can. Mineral. 41, 457–472.
Dilek, Y., Sandvol, E., 2009. Seismic structure, crustal architecture and tectonic evolution of the Anatolian African plate boundary and the Cenozoic orogenic belts in the eastern Mediterranean region. Geol. Soc. London, Special Publication 327, 127–160.
Fershtater, G.B., Krasnobaev, A.A., Bea, F., Montero, P., Borodina, N.S., 2007. Geodynamic settings and history of the Paleozoic intrusive magmatism of the central and southern Urals: results of zircon dating. Geotectonics 41, 465–486.
Forster, H., Feselfeldt, K., Kursten, M., 1972. Magmatic and orogenic evolution of the Central Iranian volcanic belt. In: International Geological Conference, Montreal, 24th section 2, 198–210.
Ghasemi, H.A., Barahmand, M., Sadeghian, M., 2011. The Oligocene basaltic lavas of east and southeast of Shahroud: implication for back-arc basin setting of Central Iran Oligo-Miocene basin. Petrology 2, 78–94 (In Persian).
Ghasemi, M., Momenzadeh, M., Yaghubpur, A., Mirshokraei, A.A., 2008. Mineralogy and textural studies of Mehdiabad Zinc-Lead Deposit-Yazd, Central Iran. Iranian J. Crystallogr. Mineral. 3, 389–404 (In Persian).
Ghazban, F., McNutt, R.H., Schwarcz, P., 1994. Genesis of sediment-hosted Zn-Pb-Ba deposits in the Irankuh District, Esfahan Area, West-Central Iran. Econ. Geol. 89, 1262–1278.
Gheshlaghi, A., 2002. Geology and Genesis of Pinavand Fluorite Mines, Northeast of Esfahan (MS.c thesis) Shiraz University, Iran, (In Persian with English abstract).
Ghorbani, M.R., 2006. Lead enrichment in Neotethyan volcanic rocks from Iran: the implications of a descending slab. Geochem. J. 40, 557–568.
Ghorbani, M.R., Bezenjani, R.N., 2011. Slab partial melts from the metasomatizing agent to adakite, Tafresh Eocene volcanic rocks, Iran. Island Arc 20, 188–202.
Gill, J.B., 1981. Orogenic Andesites and Tectonic. Springer-Verlag, Berlin, pp. 390.
Goldstein, R.H., Reynolds, T.J., 1994. Systematics of fluid inclusions in diagenetic minerals. SEPM Short C 31, 1–199.
Griffith, E.M., Paytan, A., 2012. Barite in the ocean: occurrence, geochemistry and palaeoceanographic applications. J. Sedimentol. 59, 1817–1835.
Hannington, M.D., de Ronde, C.E.J., Petersen, S., 2005, Sea-floor tectonics and submarine hydrothermal systems. Economic Geology 100th Anniversary Volume, 111–141.
Hanor, J.S., 2000. Barite-celestine geochemistry and environments of formation. In: Alpers, C.N., Jambor, J.L., Nordstrom, D.K., (Eds.), In Reviews in Mineralogy and Geochemistry-Sulfate Minerals. Mineralogical Society of America 40, Washington, D. C., 193–275.
Hashemi, F., 2016. Mineralogy, Geochemistry and genesis of Ba-Pb-Cu ore deposit in Urumieh-Dokhtar zone, East Kashan (MS.c thesis) Shahrood University of Technology, Shahrood, Iran, (In Persian with English abstract).
Herzig, P.M., Hannington, M.D., 1995. Polymetallic massive sulphides at the modern

seafloor: a review. Ore Geol. Rev. 10, 95–115.
Huston, D.L., Relvas, J.M.R.S., Gemmell, J.B., Drieberg, S., 2011. The role of granites in volcanic-hosted massive sulphide ore-forming systems: an assessment of magmatic–hydrothermal contributions. Miner. Deposita 46, 473–507.
Irvine, T.N., Baragar, W.R.A., 1971. A guide to the chemical classification of the common volcanic rocks. Can. J. Earth Sci. 8, 523–548.
Jamieson, J.W., Hanningtone, M.D., Tivey, M.K., Hansteen, T., Williamson, N.M., Stewart, M., Fietzke, J., Butterfield, D., Frische, M., Allen, L., Cousens, B., Langer, J., 2016. Precipitation and growth of barite within hydrothermal vent deposits from the Endeavour Segment, Juan de Fuca Ridge. Geochim. Cosmochim. Acta 173, 64–85.
Kananian, A., Sarjoughian, F., Nadimi, A., Ahmadian, J., Ling, W., 2014. Geochemical characteristics of the Kuh-e Dom intrusion, Urumieh-Dokhtar Magmatic Arc (Iran): implications for source regions and magmatic evolution. J. Asian Earth Sci. 90, 137–148.
Khalaj-Masoumi, M., Lotfi, M., Nazari, M., 2009. Definition of mineralization model from Tappeh Sorkh-E-Bejegan mine, Delijan, Markazi province. J. Earth Resour. 1, 33–43 (In Persian).
Kontak, D., Gize, A., Marshal, D., 2006. Structurally controlled vein barite mineralization in the maritimes basin of eastern Canada: geologic setting, stable isotopes, and fluid Inclusions. Econ. Geol. 101, 407–430.
Large, T.T., McPhie, J.Y., Gemmell, J.B., Herrmann, W., Davidson, G.J., 2001. The spectrum of ore deposit types, volcanic environments, alteration halos, and related exploration vectors in submarine volcanic successions: some examples from Australia. Econ. Geol. 96, 913–938.
Lode, S., Piercey, S.J., Squires, G.C., 2016. Role of metalliferous mudstones and detrital shales in the localization, genesis, and paleoenvironment of volcanogenic massive sulphide deposits of the Tally Pond volcanic belt, central Newfoundland, Canada. Can. J. Earth Sci. 53 (4), 387–425.
Margoum, D., Bouabdellah, M., Klügel, A., Banks, D., Castorina, F., Jébrak, M., Bozkaya, G., 2015. Pangea rifting and onward pre-Central Atlantic opening as the main ore-forming processes for the genesis of the Aouli REE-rich fluorite–barite vein system, Upper Moulouya District, Morocco. J. Afr. Earth Sc. 108, 22–39.
McDonough, W.F., Sun, S.S., 1995. The composition of the Earth. Chem. Geol. 120, 223–253.
Melekestseva, I.Yu., Tret'yakov, G.A., Nimis, P., Yuminov, A.M., Maslennikov, V.V., Maslennikova, S.P., Kotlyarov, V.A., Beltenev, V.E., Danyushevsky, L.V., Large, R., 2014. Barite-rich massive sulfides from the Semenov-1 hydrothermal field (Mid-Atlantic Ridge, 13° 30.87′ N): evidence for phase separation and magmatic input. Mar. Geol. 349, 37–54.
Muller, D., Groves, D.I., 2000. Potassic Igneous Rocks and Associated Gold-copper Mineralization. Springer-Verlag, New York.
Muller, D., Rock, N.M.S., Groves, D.I., 1992. Geochemical discrimination between shoshonitic and potassic volcanic rocks in different tectonic settings: a pilot study. Mineral. Petrol. 46, 259–289.
Nabavi, M.H., Houshmandzadeh, A., 1984. Geological Map of Kuh-e Latif, scale 1:100000. Geological Survey of Iran, No 6456, Tehran, Iran.
Nadimi, A., Konon, A., 2012. Strike-slip faulting in the central part of the Sanandaj-Sirjan Zone, Zagros Orogen, Iran. J. Struct. Geol. 40, 2–16.
Nejadhadad, M., Taghipour, B., Zarasvandi, A.R., Karimzadeh Somarin, A.R., 2016. Geological, geochemical, and fluid inclusion evidences for the origin of the Ravanj Pb–Ba–Ag deposit, north of Delijan city, Markazi Province, Iran. Turkish J. Earth Sci. 25, 179–200.
Omrani, J., Agard, P., Whitechurch, H., Benoit, M., Prouteau, G., Jolivet, L., 2008. Arc-magmatism and subduction history beneath the Zagros Mountains, Iran: a new report of adakites and geodynamic consequences. Lithos 106, 380–398.
Parsapoor, A., Khalili, M., Mackizadeh, M.A., 2009. The behaviour of trace and earth elements (REE) during hydrothermal alteration in the Rangan area (Central Iran). J. Asian Earth Sci. 34, 123–134.
Peccerillo, A., Taylor, S.R., 1976. Geochemistry of Eocene calc-alkaline volcanic-rocks from Kastamonu area, northern Turkey. Contrib. Miner. Petrol. 58, 63–81.
Pfaff, K., Hildebrandt, L.H., Leach, D.L., Jacob, D.E., Markl, G., 2010. Formation of the Mississippi Valley-type Zn-Pb-Ag deposit in the extensional setting of the upper Rhinegraben in the Wiesloch area, SW Germany. Miner. Deposita 45, 647–666.
Pourhosseini, F., 1981. Petro genesis of Iranian Plutons: a study of the Natanz and Bazman intrusive complexes (Ph.D thesis) University of Cambridge, Geological Survey of Iran, report, No 53, 315 p, (In Persian with English abstract).
Rajabi, A., Rastad, E., Canet, C., 2012. Metallogeny of Cretaceous carbonate hosted Zn–Pb deposits of Iran: geotectonic setting and data integration for future mineral exploration. Int. Geol. Rev. 54, 1649–1672.
Reuter, M., Piller, W.E., Harzhauser, M., Mandic, O., Berning, B., Rogl, F., Kroh, A., Aubry, M.B., Wielandt-Schuster, U., Hamedani, A., 2007. The Oligo-Miocene Qom Formation (Iran): evidence for an early Burdigalian restriction of the Tethyan Seaway and closure of its Iranian gateways. Int. J. Earth Sci. 98, 627–650.
Revan, M.K., Genç, Y., Maslennikov, V.V., Maslennikova, S.V., Large, R.R., Danyushevsky, L.V., 2014. Mineralogy and trace-element geochemistry of sulfide minerals in hydrothermal chimneys from the Upper-Cretaceous VMS deposits of the eastern Pontide orogenic belt (NE Turkey). Ore Geol. Rev. 63, 129–149.
Sengor, A.M.C., 1987. Tectonics of the Tethysides: orogenic collage development in a collisional setting. Annu. Rev. Earth Planet. Sci. 15, 213–244.
Shadlun, T.N., Bortnikov, N.S., Bogdanov, Yu.A., Tufar, W., Murav'ev, K.G., Gurvich, E.G., Muravitskaya, G.N., Korina, E.A., Topa, T., 1991. Mineral composition, structures and formation conditions of the modern sulfide ores in the spreading zone of the Manus basin. Geologiya Rudnukh Mestorozhdenii 5, 3–21.
Shahabpour, J., 2007. Island arc affinity of the central Iranian belt. J. Asian Earth Sci. 30, 652–665.
Stocklin, J., 1968. Structural history and tectonics of Iran: a review. Am. Assoc. Pet. Geol. Bull. 52, 1229–1258.
Taghipour, B., Moore, F., Mackizadeh, M.A., 2010. Stable isotope evidences of jarosite–barite mineralization in the Rangan rhyolitic dome NE Isfahan, Iran. Chemie der Erde 70, 377–384.
Tessalina, S.G., Jourdan, F., Belogub, E.V., 2017. Significance of Late Devonian – lower Carboniferous ages of hydrothermal sulphides and sericites from the Urals Volcanic-Hosted Massive Sulphide deposits. Ore Geol. Rev. 85, 131–139.
Torró, L., Proenza, J.A., Melgarejo, J.C., Alfonso, P., Farré de Pablo, J., Colomer, J.M., García-Casco, A., Gubern, A., Gallardo, E., Cazañas, X., Chávez, C., Del Carpio, R., León, P., Nelson, C.E., Lewis, J.F., 2016. Mineralogy, geochemistry and sulfur isotope characterization of Cerro de Maimón (Dominican Republic), San Fernando and Antonio (Cuba) lower Cretaceous VMS deposits: formation during subduction initiation of the proto-Caribbean lithosphere within a fore arc. Ore Geol. Rev. 72, 794–817.
Urabe, T., 1987. Kuroko deposit modeling based on magmatic hydrothermal theory. Mining Geol. 37, 159–175.
Verdel, C., 2009. Cenozoic Geology of Iran: An Intergrated Study of Extentional Tectonics and Related Volcanism (Ph.D Thesis) California Institute of Technology, Pasadena, California.
Verdel, C., Wernicke, B.P., Hassanzadeh, J., Guest, B., 2011. A Paleogene extensional arc flare-up in Iran. Tectonics, 30, TC3008. doi: 10.1029/2010TC002809.
Von Quadt, A.V., Erni, M., Martinek, K., Moll, M., Peytcheva, I., Heinrich, C.A., 2011. Zircon crystallization and the lifetimes of ore-forming magmatic-hydrothermal systems. Geology 39, 731–734.
Whitney, D., Evans, B., 2010. Abbreviations for names of rock-forming minerals. Am. Mineral. 95, 185–187.
Wilkinson, J.J., 2001. Fluid inclusions in hydrothermal ore deposits. Lithos 55, 229–272.
Wilson, M., 2007. Igneous Petrogenesis, A Global Tectonic Approach. Springer, Chapman and Hall, London, pp. 480.
Yeats, C.J., Hollis, S.P., Halfpenny, A., Corona, G.C., LaFlamme, C., Southam, G., Fiorentini, M., Herrington, R.J., Spratt, J., 2017. Actively forming Kuroko-type volcanic-hosted massive sulfide (VHMS) mineralization at Iheya North, Okinawa Trough, Japan. Ore Geol. Rev. 84, 20–41.